

**Antiferromagnetic ordering and chiral crystal structure transformation in Nd<sub>3</sub>Rh<sub>4</sub>Sn<sub>13</sub>**

Ami Shimoda

*Graduate School of Science, Ibaraki University, Mito, Ibaraki 310-8512, Japan*Kazuaki Iwasa \**Research and Education Center for Atomic Sciences, Ibaraki University, Tokai, Naka, Ibaraki 319-1106, Japan  
and Institute of Quantum Beam Science, Ibaraki University, Mito, Ibaraki 310-8512, Japan*

Keitaro Kuwahara

*Institute of Quantum Beam Science, Ibaraki University, Mito, Ibaraki 310-8512, Japan  
and Research and Education Center for Atomic Sciences, Ibaraki University, Tokai, Naka, Ibaraki 319-1106, Japan*Hajime Sagayama and Hironori Nakao *Institute of Materials Structure Science, High Energy Accelerator Research Organization, Tsukuba, Ibaraki 305-0801, Japan*Motoyuki Ishikado  and Akiko Nakao*Neutron Science and Technology Center, Comprehensive Research Organization for Science and Society (CROSS),  
Tokai, Naka, Ibaraki 319-1106, Japan*Seiko Ohira-Kawamura , Naoki Murai, and Takashi Ohhara *Materials and Life Science Division, J-PARC Center, Japan Atomic Energy Agency, Tokai, Ibaraki 319-1195, Japan*Yusuke Nambu *Institute for Materials Research and Organization for Advanced Studies, Tohoku University, Sendai 980-8577, Japan  
and FOREST, Japan Science and Technology Agency, Kawaguchi, Saitama 332-0012, Japan*

(Received 16 February 2024; accepted 27 March 2024; published 16 April 2024)

The detailed electronic superlattice structure of the Remeika phase compound Nd<sub>3</sub>Rh<sub>4</sub>Sn<sub>13</sub> was investigated. The material undergoes a structural phase transition at  $T_D \simeq 338$  K between the high temperature phase ( $Pm\bar{3}n$ ) and the low temperature chiral structure phase ( $I2_13$ ), which is the same symmetry change as that of the La- and Ce-based Remeika phase compounds. The inequivalent Nd-ion sites in the chiral phase are occupied by different crystalline electronic field splitting schemes of the  $4f^3$  electronic configuration with the total angular momentum  $J = 9/2$ , which results in two-sublattice antiferromagnetic ordering below  $T_N = 1.65$  K. The one-dimensional Nd-ion chains in which the magnetic moments are alternately arranged are connected via the second-neighbor triangular lattice in the chiral phase, which suggests a magnetic frustration effect.

DOI: [10.1103/PhysRevB.109.134425](https://doi.org/10.1103/PhysRevB.109.134425)**I. INTRODUCTION**

Chiral and noncentrosymmetric crystal structures have been investigated for topological electronic states as the Dirac/Weyl fermion, which is associated with an asymmetric spin-orbit coupling [1]. Time-reversal symmetry breaking also plays a role in producing the topological states in addition to a spatial-symmetry breaking effect. The Dirac/Weyl fermion carriers characterized by a linear massless dispersion relation are proposed to cause unconventional magnetic correlations because of modifications of the Ruderman-Kittel-Kasuya-Yosida (RKKY) and Dzyaloshinskii-Moriya (DM) interactions by the asymmetric spin-orbit coupling [2].

Recently, the so-called Remeika phase of the 3-4-13 class of materials was a candidate system for investigating topological electronic phenomena. Series compounds have been considered to crystallize in the Yb<sub>3</sub>Rh<sub>4</sub>Sn<sub>13</sub>-type structure (centrosymmetric space group  $Pm\bar{3}n$  (No. 223) with a lattice constant of approximately 9.6–9.7 Å) [3–9]. A heavy-fermion (HF) state in the Ce-based Remeika phase materials has been proposed, which can be attributed to the Kondo effect owing to hybridization between the  $f$  electrons and conduction electrons, as discussed for Ce<sub>3</sub>Pt<sub>4</sub>In<sub>13</sub> [10]. The values of specific heat divided by the temperatures of Ce<sub>3</sub>Co<sub>4</sub>Sn<sub>13</sub> [11–14], Ce<sub>3</sub>Rh<sub>4</sub>Sn<sub>13</sub> [12,15,16], and Ce<sub>3</sub>Ir<sub>4</sub>Sn<sub>13</sub> [17–19] reach approximately 4, 0.4, and 0.67 J/(K<sup>2</sup> mol Ce) at low temperatures, respectively. The electrical resistivity data of these Ce-based compounds is less dependent on temperature. These phenomena can be explained by the HF scenario and

\*kazuaki.iwasa.ifrc@vc.ibaraki.ac.jp

the Kondo semimetal formation. Furthermore,  $\text{Ce}_3\text{Tr}_4\text{Sn}_{13}$  ( $\text{Tr} = \text{Co}, \text{Rh}, \text{and Ir}$ ) undergo the structural phase transitions from the high-temperature I phase to the low temperature I' phase at 160, 350, and approximately 600 K, respectively [20–22]. The I phase belongs to the originally proposed cubic space group  $Pm\bar{3}n$  [3–5]. The I'-phase crystal structure exhibits a chiral symmetry in the cubic space group  $I2_13$  (No. 199) with lattice constants of 19.2–19.4 Å, which is associated with a superlattice formation characterized by the wave vector  $\mathbf{q}_L = (1/2, 1/2, 0)$  [20–23]. Therefore, as recently established for  $\text{Ce}_3\text{Rh}_4\text{Sn}_{13}$  [24],  $\text{Ce}_3\text{Tr}_4\text{Sn}_{13}$  ( $\text{Tr} = \text{Co}, \text{Rh}, \text{and Ir}$ ) are Weyl-Kondo semimetals, as discussed in previous studies [25–27].  $\text{La}_3\text{Tr}_4\text{Sn}_{13}$  ( $\text{Tr} = \text{Co}, \text{Rh}, \text{and Ir}$ ) also undergo the same structural phase transition as that in the Ce-based compounds [20–22, 28, 29]. Superconductivity below approximately 2.5 K in these La-based materials is expected to be a signature of a parity-mixing Cooper pairing mechanism [30, 31].

Some of the Remeika phases exhibit magnetic ordering, along with crystal structure superlattice formation.  $\text{Nd}_3\text{Co}_4\text{Sn}_{13}$  is characterized by the  $\mathbf{q}_L = (1/2, 1/2, 0)$  superlattice below 124 K [32], which is expected to be the same structure as that in the I' phase of  $\text{Ce}_3\text{Tr}_4\text{Sn}_{13}$ . In addition, an antiferromagnetic (AFM) ordered structure below 2.4 K has been revealed using neutron diffraction (ND), which is characterized by the wave vector  $\mathbf{q}_M = (0, 0, 0)$  [33]. Structural and magnetic ordering phase transitions have also been reported for  $\text{Gd}_3\text{Ir}_4\text{Sn}_{13}$  [34] and  $\text{Eu}_3\text{Ir}_4\text{Sn}_{13}$  [35]. Therefore, the electronic states resulting from a combination of time-reversal-symmetry and spatial symmetry breaking (chiral) in the magnetic Remeika phases are controversial.

This study reveals that  $\text{Nd}_3\text{Rh}_4\text{Sn}_{13}$ , for which no detailed structural and electronic properties have been investigated, exhibits a characteristic 4f-electron superlattice seen in successive formations of a chiral structure at 338 K and an AFM order at 1.65 K. A part of this study has been published in a previous paper [36].

## II. EXPERIMENTAL DETAILS

Single-crystalline samples (dimensions of 5 mm at maximum) of  $\text{Ln}_3\text{Rh}_4\text{Sn}_{13}$  ( $\text{Ln} = \text{La}$  and  $\text{Nd}$ ) were synthesized using the molten Sn-flux method [6–8, 13]. The starting materials [ $\text{Ln}$  (3N),  $\text{Rh}$  (4N), and  $\text{Sn}$  (5N)] were loaded in an alumina crucible that was sealed in an evacuated silica tube. The tube was heated to 1273 K, and cooled slowly. Excess Sn was removed using hydrochloric acid.

Synchrotron x-ray diffraction experiments were conducted using a four-circle single-crystal diffractometer installed at BL-4C of the Photon Factory (PF) in the High Energy Accelerator Organization (KEK). A helium gas closed-cycle refrigerator was used to cool the samples down to 5 K. An x-ray energy of 12 keV was selected to measure the order-parameter evolution as a function of temperature. A structural refinement study was conducted for small single-crystal samples whose dimensions were approximately 40 μm on the imaging plate x-ray diffractometer at BL-8A of PF. The x-ray incident energy of 18 keV was selected. The sample temperatures were controlled by using a nitrogen-gas-blow cryostat. Structural analysis was performed using the fol-

lowing software: RIGAKU RAPID for evaluating the structure factors, SIR2014 for a direct method, and SHELX for refinement analysis in the WINGX suite [37].

Magnetic property measurements between 1.9 and 300 K were performed using a superconducting quantum interference device (SQUID) magnetometer (MPMS of Quantum Design, Inc.) installed at the Neutron Science and Technology Center, Comprehensive Research Organization for Science and Society (CROSS Tokai).

Inelastic neutron scattering (INS) experiments were conducted using the pulsed-cold-neutron disk chopper spectrometer AMATERAS installed at the beamline BL14 of the Materials and Life Science Experimental Facility (MLF), J-PARC [38]. The spectra of the  $\text{Ln}_3\text{Rh}_4\text{Sn}_{13}$  ( $\text{Ln} = \text{La}$  and  $\text{Nd}$ ) specimens were measured to extract the 4f-electron contribution from the difference between the data of these two compounds. An incident neutron energy of  $E_i = 23.625$  meV was selected via the chopper combination with an energy resolution of 1.262 meV estimated from the full width at half maximum at the elastic scattering positions. Analysis of the time-of-flight (ToF) neutron spectral data was performed using the UTSUSEMI software suite [39].

Powder ND measurements were performed using the diffractometer HERMES installed at the T1-3 beam hole of Japan Research Reactor 3 (JRR-3) at the Japan Atomic Energy Agency, Tokai. An incident neutron wavelength of 2.1974 Å was selected using a Ge analyzer. The sample temperature was controlled by using a  $^3\text{He}$  closed cycle refrigerator. The neutron single-crystal diffractometer SENJU installed at BL18 of MLF in J-PARC was also used to investigate a single-crystal sample with an approximate diameter of 3 mm, which was cooled to temperatures between 0.3 and 2.5 K by using a  $^3\text{He}$  cryostat [40–43].

## III. RESULTS

### A. X-ray diffraction for structural phase transition

$\text{Nd}_3\text{Rh}_4\text{Sn}_{13}$  undergoes a structural phase transition, as reported in a recent study [36]. Figure 1(a) depicts single-crystal x-ray diffraction data for the scattering-vector  $\mathbf{Q} = (6.5, 0.5, 0)$  obtained using BL-4C at PF, with Miller indices relative to the unit cell dimension of 9.68 Å. The inset figure shows the temperature evolution of the intensity profile at  $\mathbf{Q} = (6.5, 0.5, 0)$  of  $\text{Nd}_3\text{Rh}_4\text{Sn}_{13}$ . The abscissa represents the reduced wave number along the  $[0, 1, 0]$  axis of the two-dimensional detector. The intensity was recorded through the rocking-curve scan; thus, the integrated intensity can be evaluated by summing the detected counts. The main figure shows the temperature dependence of the integrated intensity, which is normalized by that of the fundamental reflection at  $\mathbf{Q} = (8, 0, 0)$  to correct the variation in the mutual relationship between the incident x-ray and the sample position. The diffraction peak at  $\mathbf{Q} = (6.5, 0.5, 0)$  is gradually enhanced with decreasing temperature, indicating a second-order structural transition characterized by  $\mathbf{q}_L = (1/2, 1/2, 0)$ , as observed also for  $\text{Ln}_3\text{Tr}_4\text{Sn}_{13}$  ( $\text{Ln} = \text{La}$  and  $\text{Ce}$ ;  $\text{Tr} = \text{Co}, \text{Rh}, \text{and Ir}$ ) and  $\text{Nd}_3\text{Co}_4\text{Sn}_{13}$ . The data points above 300 K were reproduced by the critical form of  $(1 - T/T_D)^{2\beta}$  with the exponent  $\beta = 0.484(4)$  and the transition temperature  $T_D = 338(1)$  K.

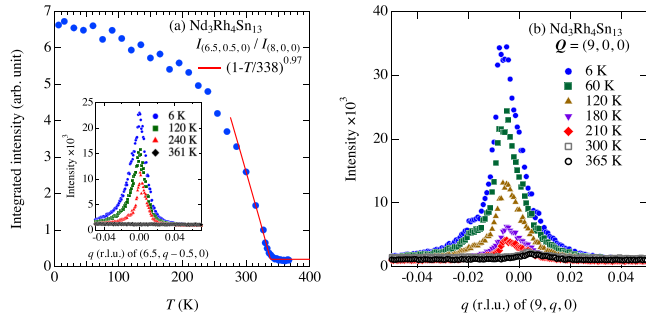


FIG. 1. (a) Inset figure shows scan profiles at  $\mathbf{Q} = (6.5, 0.5, 0)$  of  $\text{Nd}_3\text{Rh}_4\text{Sn}_{13}$  at selected temperatures obtained on the two-dimensional detector of BL-4C. The main panel shows the temperature dependence of integrated intensity at  $\mathbf{Q} = (6.5, 0.5, 0)$ , which is normalized by that of the fundamental reflection at  $\mathbf{Q} = (8, 0, 0)$ . The solid line indicates a fitting result based on a critical behavior expressed as  $(1 - T/T_D)^{2\beta}$  with  $\beta = 0.484(4)$  and  $T_D = 338(1)$  K. (b) Scan profiles at  $\mathbf{Q} = (9, 0, 0)$  of  $\text{Nd}_3\text{Rh}_4\text{Sn}_{13}$  at selected temperatures obtained on the two-dimensional detector of BL-4C.

Figure 1(b) shows the diffraction peak at  $\mathbf{Q} = (9, 0, 0)$  measured using the BL-4C diffractometer. A very small peak is observed in the higher temperature region, which can be explained by unexpected background on the wide detector. Thus, the data are consistent with those obtained under the forbidden reflection condition  $\mathbf{Q} = (h, 0, 0)$ , with  $h$  odd, of the suggested cubic crystal structure categorized in the space group  $Pm\bar{3}n$  (No. 223). The peak intensity increases with decreasing temperature. Such a characteristic behavior in the  $I'$  phase is discussed in the crystal structure refinement described later.

Figure S.1 in the Supplemental Material shows the x-ray diffraction spots of  $\text{Nd}_3\text{Rh}_4\text{Sn}_{13}$  detected on the imaging plate of BL-8A at PF, KEK [44]. The data measured at 360 K (left panel) show only fundamental peaks, indexed by integers, with respect to the cubic unit cell with  $a = 9.6793$  Å. At 200 K (right panel), additional superlattice spots indexed by  $q_L = (1/2, 1/2, 0)$  appear, which is consistent with the BL-4C data. Subsequently, these results are analyzed to refine the crystal structure.

## B. Magnetic susceptibility

Figure 2 shows the data of magnetization,  $M$ , divided by the applied magnetic fields,  $H$ , for  $\text{Nd}_3\text{Rh}_4\text{Sn}_{13}$ . The background data measured without the samples were subtracted to extract only the sample magnetization only. The inverse of  $M/H$  [Fig. 2(a)] above 100 K is reproduced by the Curie-Weiss law with an effective magnetic moment value of  $\mu_{\text{eff}} = 3.64\mu_B/\text{Nd}$  and the Weiss temperature of  $\Theta = -13.7$  K.  $\mu_{\text{eff}}$  is very close to that of the expected value  $3.62\mu_B/\text{Nd}$  for the  $\text{Nd}^{3+} 4f^3$  configuration; thus, the magnetic moment is located only at the Nd sites. Figure 2(b) shows a low-temperature part of  $M/H$  [36]. Note that an increase in  $M/H$  with decreasing temperature is suppressed below approximately 3 K, and  $M/H$  is nearly saturated at 2 K above the AFM ordering temperature, as discussed subsequently.

## C. Inelastic neutron scattering

To reveal split level schemes under crystalline electric fields (CEF) and the electronic ground state of  $\text{Nd}_3\text{Rh}_4\text{Sn}_{13}$ ,

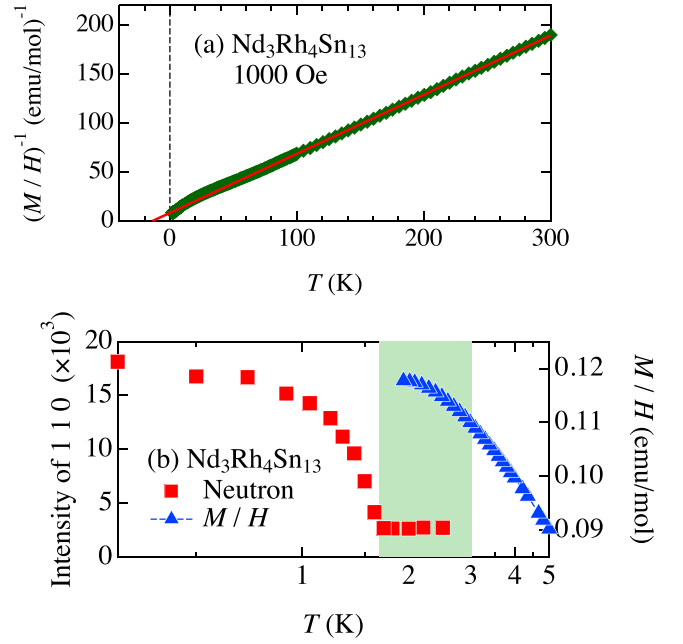


FIG. 2. (a) Inverse of  $M/H$  data of  $\text{Nd}_3\text{Rh}_4\text{Sn}_{13}$  at  $B = 0.1$  T. The solid line indicates a fitted result based on the Curie-Weiss law. (b) The blue triangles with the right ordinate indicate low-temperature  $M/H$  data, and the red squares with the left ordinate indicate ND intensity of  $(1\ 1\ 0)$  [36].

INS measurements were conducted using the neutron ToF spectrometer AMATERAS installed at BL14 of J-PARC. Figure 3 shows measured data integrated in the range of scattering-vector magnitude  $Q = 1.0\text{--}2.0$  Å<sup>-1</sup>, which was obtained for the  $E_i = 23.625$  meV setup. The measured data of the reference material  $\text{La}_3\text{Rh}_4\text{Sn}_{13}$  were subtracted from those of  $\text{Nd}_3\text{Rh}_4\text{Sn}_{13}$  to extract only the magnetic scattering component, and the data were transformed to the scattering function defined as  $S(\mathbf{Q}, E) = (k_f/k_i)^{-1} d^2\sigma/d\Omega dE_f$ , where  $k_f$ ,  $k_i$ , and  $d^2\sigma/d\Omega dE_f$  denote the outgoing neutron wave number, incident neutron wave number, and differential cross section, respectively. The details of the data correction are shown in the Supplemental Material [44]. Sharp peaks are observed between 6 and 18 meV, which can be attributed to the CEF excitation peaks of the Nd ions. Considering a resolution width of 1.262 meV for the  $E_i = 23.625$  meV setup, we can assign peaks at 6.5, 8.2, 8.9, 10.0, 11.3, 12.2, and 14.9 meV. However, these peaks cannot be attributed to the single  $\text{Nd}^{3+} 4f^3$  configuration with the total angular momentum  $J = 9/2$ , which indicates four excitation peaks at low temperatures between five Kramers doublet CEF levels. Therefore, the observed spectrum should be analyzed by considering the structural superlattice revealed by the x-ray diffraction.

## D. Neutron diffraction for magnetic ordering

### 1. Powder sample study

The red circles in Fig. 4 indicate the powder ND data of  $\text{Nd}_3\text{Rh}_4\text{Sn}_{13}$  at 0.64 K measured at HERMES of JRR-3. The overall pattern is consistent with the crystal structure observed in the synchrotron x-ray diffraction patterns described above, which are indicated by green vertical bars. In addition, the

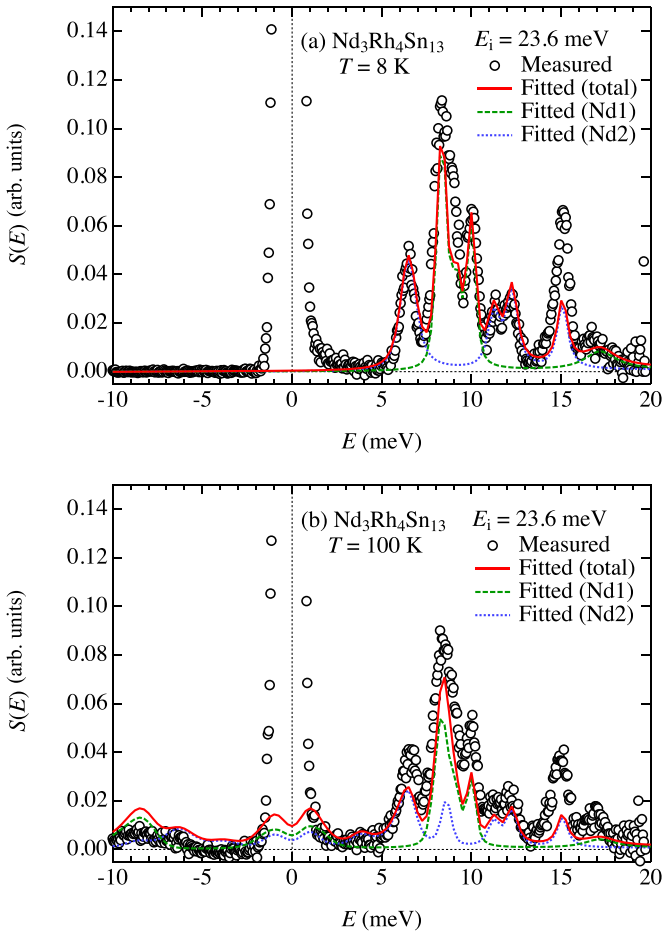


FIG. 3. The black circles indicate magnetic scattering functions  $S(E)$  of  $\text{Nd}_3\text{Rh}_4\text{Sn}_{13}$  measured at 8 K (a) and 100 K (b), which were evaluated from intensity integration in the range of  $Q = 1.0\text{--}2.0 \text{ \AA}^{-1}$ . The red solid lines are fitted results based on the two inequivalent CEF scheme models (the blue dotted lines for Nd1 and the green broken lines for Nd2).

data contain several tiny reflections enhanced at lower temperatures. The left inset shows the data taken in the range  $2\theta = 8\text{--}35^\circ$  measured at 0.64 K (red circles) and 2.0 K (green line). The reflections at  $(1\ 0\ 0)$ ,  $(1\ 1\ 0)$ ,  $(1\ 1\ 1)$ ,  $(2\ 1\ 0)$ , and  $(2\ 1\ 1)$  enlarge at 0.64 K. The observed peak evolution is the same as that reported in the study on  $\text{Nd}_3\text{Co}_4\text{Sn}_{13}$ , which exhibits the AFM ordering below 2.4 K characterized by the wave vector  $\mathbf{q}_M = (0, 0, 0)$  [33]. The data points appearing in the  $2\theta$  ranges ( $55.00^\circ\text{--}57.00^\circ$ ,  $65.00^\circ\text{--}67.00^\circ$ ,  $99.80^\circ\text{--}101.30^\circ$ ,  $128.50^\circ\text{--}130.20^\circ$ , and  $140.50^\circ\text{--}142.50^\circ$ ) originate from the scattering of the aluminum sample container, as indicated by Al  $hkl$ . Subsequently, we perform the Rietveld analysis to derive the AFM ordered structure in  $\text{Nd}_3\text{Rh}_4\text{Sn}_{13}$ .

## 2. Single-crystal sample study

To gain deeper insights into the magnetic ordering phase transition, we conducted single-crystal ND measurements. The two-dimensional detectors of SENJU at BL18 of J-PARC were successfully used to detect the intensity enhancement in the low temperature range, not only at the reciprocal lattice points with the integer indices which were observed in the

powder ND study, but also at those with the half-integer reflections, which are at the same positions as the crystal superlattice reflections. The temperature dependencies of the integrated intensities at the scattering vectors  $\mathbf{Q} = (1, 1, 0)$  and  $(2, 2, 3)$  are shown in Fig. 5(a). The increment in these integer reflections is consistent with the powder ND results. The magnetic ordering temperature is estimated to be  $T_N = 1.65$  K. Note that the magnetic susceptibility saturation behavior [Fig. 2(b)] appears clearly above the long-range ordering temperature  $T_N$ . We also detected the AFM reflections at  $\mathbf{Q} = (1, 3, 3)$  and  $\mathbf{Q} = (3, 1, 3)$ , as shown in Figs. 5(b) and 5(c), respectively. In addition to these stronger magnetic reflections, significantly smaller reflections were observed at the half-integer superlattice points; for example,  $\mathbf{Q} = (1, 5/2, 5/2)$ ,  $(5/2, 1, 5/2)$ ,  $(3/2, 3, -3/2)$ , and  $(3/2, 3/2, 3)$  shown in Figs. 5(b) and 5(c). Although the intensities are less by one order of magnitude than the stronger magnetic reflections, the systematic peak appearance at the half-integer positions below  $T_N$  supports the superlattice associated with the two inequivalent magnetic moments, as described later in detail.

## IV. ANALYSIS

### A. Crystal structure

Detailed crystal structure analysis was performed on the basis of the oscillation photograph data measured at BL-8A, PF. The structural analysis results are summarized in the Supplemental Material [44].

The measurement data at 360 K above  $T_D$  shown in Fig. S.1 in the Supplemental Material comprise reflections indexed by the cubic structure with a lattice constant of  $9.6793 \text{ \AA}$ . Structural analysis based on the space group  $Pm\bar{3}n$  and anisotropic atomic displacement factors produce refinement factors  $R_1 = 1.83\%$  and  $wR_2 = 4.54\%$  and the goodness-of-fit parameter  $S = 1.140$ , as summarized in Table S.1. The results confirm the validity of the structural refinement. The determined crystal structure is shown in Fig. S.2.

We also analyzed the data obtained at 200 K in the  $I'$  phase. As shown in the right panel of Fig. S.1, additional superlattice spots indexed by  $\mathbf{q}_L = (1/2, 1/2, 0)$  appear. The diffraction spots did not exhibit distinct splitting below  $T_D$ , thus the second-order structural transformation occurred without multidomain formation to tetragonal or lower symmetries. The collected data points are best indexed by the body-centered cubic (bcc) symmetry, which doubles the unit cell along the three equivalent principal axes. As a consequence of the second-order transition from the high-temperature space group  $Pm\bar{3}n$ , the following bcc subgroups were examined:  $I23$  (No. 197),  $I2_13$  (No. 199),  $Im\bar{3}$  (No. 204),  $Ia\bar{3}$  (No. 206),  $I4_132$  (No. 214),  $Ia\bar{3}d$  (No. 230), and  $I\bar{4}3d$  (No. 220). The analysis of  $I2_13$  produces the refinement factors  $R_1 = 2.93\%$ ,  $wR_2 = 8.20\%$ , and  $S = 1.111$ , which are satisfactory to conclude a successful structural refinement. Analysis of the same dataset based on  $I23$  (No. 197),  $Im\bar{3}$  (No. 204), and  $Ia\bar{3}$  (No. 206) produced worse refinement factors than that for  $I2_13$ . The space groups  $Ia\bar{3}d$  (No. 230),  $I\bar{4}3d$  (No. 220), and  $I4_132$  (No. 214) possess the reflection condition of  $\mathbf{Q} = (h, 0, 0)$  with  $h = 4n$ , which is not consistent with the observation of peak at  $\mathbf{Q} = (9, 0, 0)$ , as shown in Fig. 1(b),

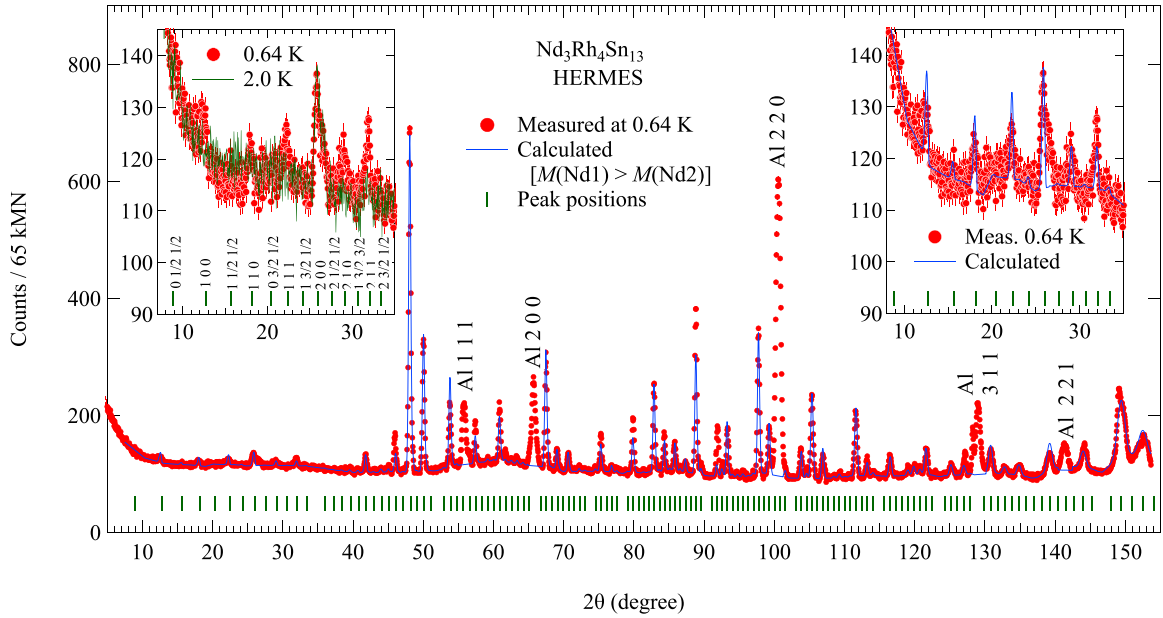


FIG. 4. The red circles and the green lines in the left inset indicate powder ND data of  $\text{Nd}_3\text{Rh}_4\text{Sn}_{13}$  at 0.64 and 2.0 K, respectively. The blue solid lines indicate the calculated results of the Rietveld analysis for the AFM structure. The green vertical bars indicate the peak positions for the nuclear and magnetic scattering.

which corresponds to  $\mathbf{Q} = (18, 0, 0)$  with respect to the superlattice structure in the  $I'$  phase. Hence, it is concluded that the low-temperature  $I'$ -phase crystal structure of  $\text{Nd}_3\text{Rh}_4\text{Sn}_{13}$  exhibits the  $I2_13$  symmetry.

The optimal  $I2_13$  space group is a chiral cubic structure. The two enantiomer structures shown in Fig. 6, which were drawn using VESTA [45], appear as a twin structure because of the nonzero Flack parameter. The large blue and green atoms correspond to two inequivalent Wyckoff sites of Nd ions with different orientations of the surrounding Sn atoms. The nearest neighbor Nd ions form one-dimensional chains along the cubic principal axes. The rotation directions of these Nd-ion chains with respect to the  $[1\ 1\ 1]$  axis in these enantiomers are opposite to each other, and they form a pair of handedness.

### B. CEF level scheme

Hereafter, the INS data are analyzed by calculating the magnetic scattering function  $S(E)$  based on the CEF Hamil-

tonian. The local symmetry at the Nd-ion site in the  $I'$ -phase structure ( $I2_13$ ) is  $C_1$ , which is lower than that of the  $D_{2d}$  point group for the I-phase structure ( $Pm\bar{3}n$ ) above  $T_D$ . However, we attempted to extract the CEF schemes using the CEF Hamiltonian terms of  $D_{2d}$  because of the small atomic displacements across  $T_D$ ; this method was also applied to the data analysis of  $\text{Ce}_3\text{Tr}_4\text{Sn}_{13}$  ( $\text{Tr} = \text{Co}, \text{Rh}, \text{and Ir}$ ) [23,24,46]. The CEF Hamiltonian for the  $\text{Nd}^{3+} 4f^3$  configuration is expressed by the  $D_{2d}$  form as follows:

$$\mathcal{H}_{\text{CEF}} = W \left[ x_1 O_2^0 + \frac{x_2}{60} O_4^0 + \frac{x_3}{12} O_4^4 + \frac{x_4}{1680} O_6^0 + \frac{1 - |x_1| - |x_2| - |x_3| - |x_4|}{240} O_6^4 \right], \quad (1)$$

where the  $O_m^n$  represent Stevens operators [47]. Using a set of basis wave functions for the total angular momentum  $J = 9/2$  for the  $\text{Nd}^{3+} 4f^3$  configuration, we diagonalized this

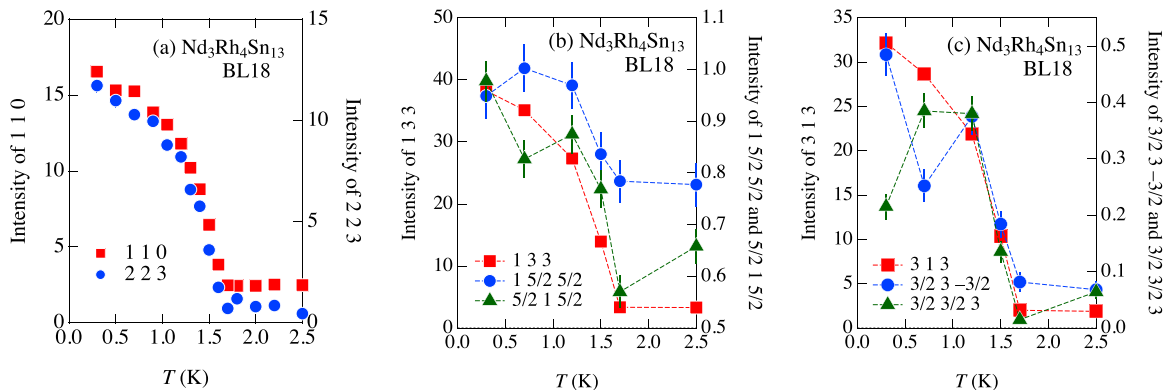


FIG. 5. Temperature dependencies of integrated intensities of ND from  $\text{Nd}_3\text{Rh}_4\text{Sn}_{13}$  at (a)  $(1\ 1\ 0)$  and  $(2\ 2\ 3)$ , (b)  $(1\ 3\ 3)$ ,  $(1\ 5/2\ 5/2)$ , and  $(5/2\ 1\ 5/2)$ , and (c)  $(3\ 1\ 3)$ ,  $(3/2\ 3 - 3/2)$ , and  $(3/2\ 3/2\ 3)$ .

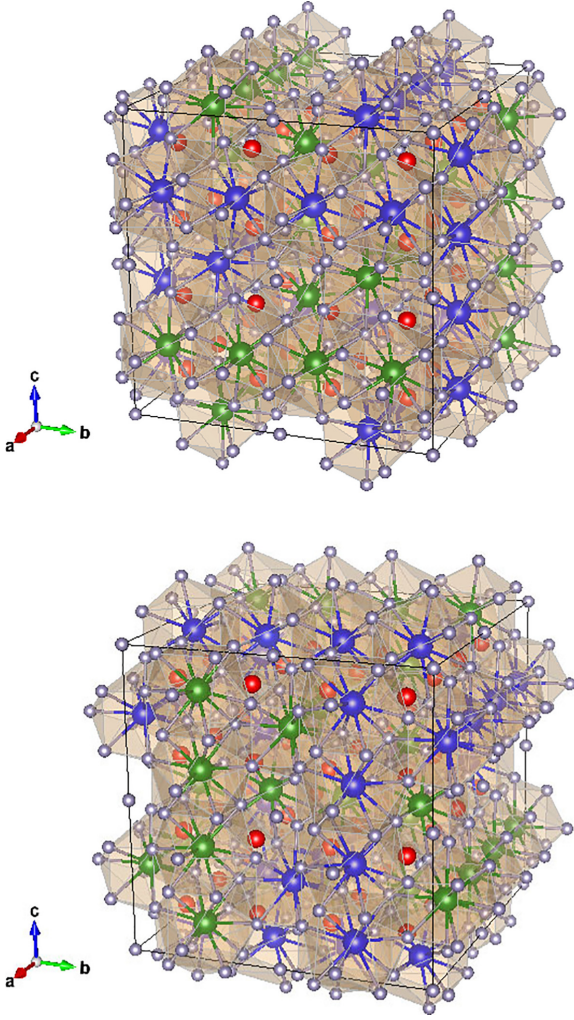


FIG. 6. Two enantiomers of  $I2_3$  chiral cubic structures of  $\text{Nd}_3\text{Rh}_4\text{Sn}_{13}$ , which were determined from the BL-8A data. The large blue atoms and green atoms correspond to two inequivalent Wyckoff sites of Nd ions. The small red circles and grey circles indicate the Rh and Sn atoms, respectively. Atomic coordinates are listed in Table S.3 of the Supplemental Material [44]. The views were drawn using VESTA [45].

Hamiltonian to obtain the eigenfunctions of the Kramers doublets: two  $\Gamma_6$  doublets and three  $\Gamma_7$  doublets. The scattering function is expressed as  $S(Q, E) = [n(E) + 1]\chi''_{\text{CEF}}(Q, E)$ , where  $\chi''_{\text{CEF}}(Q, E)$  denotes the imaginary part of the generalized magnetic susceptibility and  $n(E)$  denotes the Bose-Einstein distribution function. According to the literature [48,49],  $\chi''_{\text{CEF}}(Q, E)$  for the CEF splitting state is represented as follows:

$$\chi''_{\text{CEF}}(Q, E) \propto f^2(Q)E \frac{1}{Z} \times \left[ \sum_{m,n}^{(E_m=E_n)} |\langle n | \mathbf{J}_\perp | m \rangle|^2 \frac{e^{-\frac{E_m}{k_B T}}}{k_B T} F_{mn}(E) + \sum_{m,n}^{(E_m \neq E_n)} |\langle n | \mathbf{J}_\perp | m \rangle|^2 \frac{e^{-\frac{E_m}{k_B T}} - e^{-\frac{E_n}{k_B T}}}{E_n - E_m} F_{mn}(E) \right], \quad (2)$$

where  $f(Q)$  denotes the magnetic form factor.  $E_m$  and  $E_n$  denote the respective energy eigenvalues of the initial and final states,  $|m\rangle$  and  $|n\rangle$ , which are relevant to the scattering process due to the dipole operator  $\mathbf{J}_\perp$ .  $Z$  represents the partition function. We assumed the Lorentzian spectral function  $F_{mn}(E) = \gamma_{mn}/[(E - \Delta_{mn})^2 + \gamma_{mn}^2]$ , with  $\Delta_{mn} = E_n - E_m$ . As mentioned above, the INS spectra composed of the seven excitation peaks shown in Fig. 3 are not explained by a single CEF scheme of the  $\text{Nd}^{3+} 4f^3$  electronic configuration that produces four excitations from the doublet ground state to the excited doublet states at a significantly low temperature. This problem can be solved by taking two inequivalent CEF schemes corresponding to the two  $Ln$ -ion Wyckoff sites Nd1 and Nd2 in the  $I'$  phase, as performed in the analysis of  $\text{Ce}_3\text{Tr}_4\text{Sn}_{13}$  ( $\text{Tr} = \text{Co}, \text{Rh}, \text{and Ir}$ ) [23,24,46]. We performed a systematic search for the CEF-level schemes within the space of the two sets of CEF parameters,  $W, x_1, x_2, x_3,$  and  $x_4$ , with a constraint of the same site multiplicity for Nd1 and Nd2 in the  $I'$  phase. In particular, the observed result that no distinct additional peak appeared below 5 meV, even at 100 K, was in sharp contrast to a general feature of the CEF spectrum because transitions between excited CEF levels are expected to appear. Considering such key features of the INS spectra, we searched for the sets of CEF parameters that reproduce the seven peaks without strong peaks below 5 meV at 100 K. After obtaining the candidate parameter sets, a least-squares fitting based on the two schemes, both represented by Eq. (2) and the Lorentzian  $F_{mn}(E)$ , to the obtained data was performed. To evaluate the excitation-peak width, we incorporated a procedure for convolution of the spectrometer resolution, which was estimated by fitting the  $E = 0$  incoherent scattering part before performing the INS part analysis. The resolution at  $E > 0$  was simply assumed to be proportional to  $(1 - E/E_i)^{3/2}$  [50,51].

The fitted results are indicated by the red solid lines in Fig. 3, which comprise the Nd1 (blue dotted lines) and Nd2 (green broken lines) components. The excitation peak positions are well reproduced, whereas the intensities are not fully consistent with the measured data. The discrepancy is caused by the assumed CEF Hamiltonian [Eq. (1)] for the  $D_{2d}$  point group, which exhibits higher symmetry than the actual  $C_1$  point group in the  $I'$  phase ( $I2_3$ ). However, the analysis supports the fact that the two inequivalent CEF schemes are necessary to account for the spectra at 8 and 100 K. The resultant CEF parameters, the eigenstates, and the energy eigenvalues are listed in Table I. The CEF ground state wave functions of Nd1 and Nd2 have the magnetic moment eigenvectors  $(0.15, 0.12, 1.48)\mu_B/\text{Nd}$  and  $(0.08, 0.08, 0.81)\mu_B/\text{Nd}$ , respectively. These magnetic moment magnitudes are compared with the analysis result of the magnetic ordered structure.

### C. Magnetic structure

The Rietveld analysis method using the FULLPROF software suite [52] was applied to the powder ND data at 0.64 K (Fig. 4) to derive a magnetic ordered structure below  $T_N = 1.65$  K characterized by the wave vector  $\mathbf{q}_M = (0, 0, 0)$ . The crystal structural parameters (atomic positions and thermal parameters) were fixed to those determined in the afore-

TABLE I. The CEF parameters ( $W$ ,  $x_1$ ,  $x_2$ ,  $x_3$ ,  $x_4$ ), the eigenstate wave functions, and the energy eigenvalues (meV) at the Nd1 and Nd2 sites, which were determined by the least-squares fitting analysis of the  $E_i = 23.6$  meV dataset.

CEF scheme	Nd1	Nd2
$W$ (meV)	0.118(3)	0.159(1)
$x_1$	0.137(7)	-0.691(8)
$x_2$	-1.07(3)	-0.425(3)
$x_3$	0.207(4)	-0.384(5)
$x_4$	0.98(2)	0.571(7)
ground state	$0.044 \pm 7/2\rangle + 0.860 \mp 1/2\rangle + 0.508 \mp 9/2\rangle$	$0.184 \pm 7/2\rangle + 0.597 \mp 1/2\rangle + 0.780 \mp 9/2\rangle$
1st ex. state	$-0.889 \pm 3/2\rangle + 0.457 \mp 5/2\rangle$ , 8.34	$0.935 \pm 7/2\rangle + 0.138 \mp 1/2\rangle - 0.326 \mp 9/2\rangle$ , 6.47
2nd ex. state	$0.955 \pm 7/2\rangle + 0.114 \mp 1/2\rangle - 0.275 \mp 9/2\rangle$ , 9.15	$-0.847 \pm 3/2\rangle + 0.532 \mp 5/2\rangle$ , 11.25
3rd ex. state	$0.817 \pm 9/2\rangle - 0.497 \pm 1/2\rangle + 0.294 \mp 7/2\rangle$ , 10.00	$-0.533 \pm 9/2\rangle + 0.790 \pm 1/2\rangle - 0.302 \mp 7/2\rangle$ , 12.25
4th ex. state	$-0.876 \pm 5/2\rangle - 0.450 \mp 3/2\rangle$ , 17.13	$-0.532 \pm 3/2\rangle - 0.847 \mp 5/2\rangle$ , 15.07

mentioned synchrotron x-ray diffraction analysis for the data taken at 200 K to avoid divergence of the fitting procedure, and we optimized the magnetic moment amplitudes and the scale factor to reproduce the intensity. The previously proposed AFM model for  $\text{Nd}_3\text{Co}_4\text{Sn}_{13}$  [33], which corresponds to the irreducible representation  $\Gamma_7$  provided in the BASIREPS program [52], is applied to the present data analysis for  $\text{Nd}_3\text{Rh}_4\text{Sn}_{13}$  because similar diffraction patterns are observed in these Nd-based compounds. The nearest-neighbor Nd-ion magnetic moments are aligned alternately along the three orthogonal cubic axes, which are connected via the second neighbors. However, because of the crystallographically inequivalent Nd-ion sites in the  $I2_13$  space group structure, two inequivalent magnetic moments associated with the CEF level schemes at Nd1 and Nd2 should be considered. According to the irreducible representation analysis of  $I2_13$  provided in BASIREPS, we found that the  $\mathbf{q}_M = (0, 0, 0)$  AFM structure is represented by  $3\Gamma_1^{(1)} + 3\Gamma_2^{(2)} + 9\Gamma_3^{(3)}$ , where the superscript numbers indicate dimensions of the irreducible representations, which are summarized in Table S.4 of the Supplemental Material [44]. The present AFM structure model for  $\text{Nd}_3\text{Rh}_4\text{Sn}_{13}$  is categorized in  $\Gamma_3^{(3)}$ . We assumed simply the same magnetic moment components along the cubic principal axes, which correspond to coefficients of the basis vectors  $\psi_{11}$ ,  $\psi_{13}$ ,  $\psi_{20}$ ,  $\psi_{22}$ ,  $\psi_{29}$ ,  $\psi_{31}$  listed in Table S.4 of the Supplemental Material [44]. In the Rietveld analysis, the data points of aluminum diffraction originating from the sample container were excluded from the fitting procedure. The fitted result is shown by a blue solid line, which reproduces the measured data. The reliability factors for fitting quality (not corrected for background in FULLPROF) are  $R_p = 3.74\%$ ,  $R_{wp} = 5.94\%$ , and  $R_{exp} = 1.75\%$ . Figure 7 shows the determined AFM structure of the two inequivalent Nd sublattices. The upper panel shows the ordered magnetic moments indicated by red arrows, which are aligned alternately along the nearest neighbor Nd-ion chain. The Nd1 sites indicated by blue circles carry a larger magnetic moment of  $2.15(19)\mu_B$ , and the Nd2 sites indicated by green circles carry a smaller magnetic moment of  $1.12(19)\mu_B$ . Such an inequivalent ordered magnetic moment structure is consistent with the two CEF-level schemes determined in the INS study and the small magnetic diffraction peaks at the half-integer positions

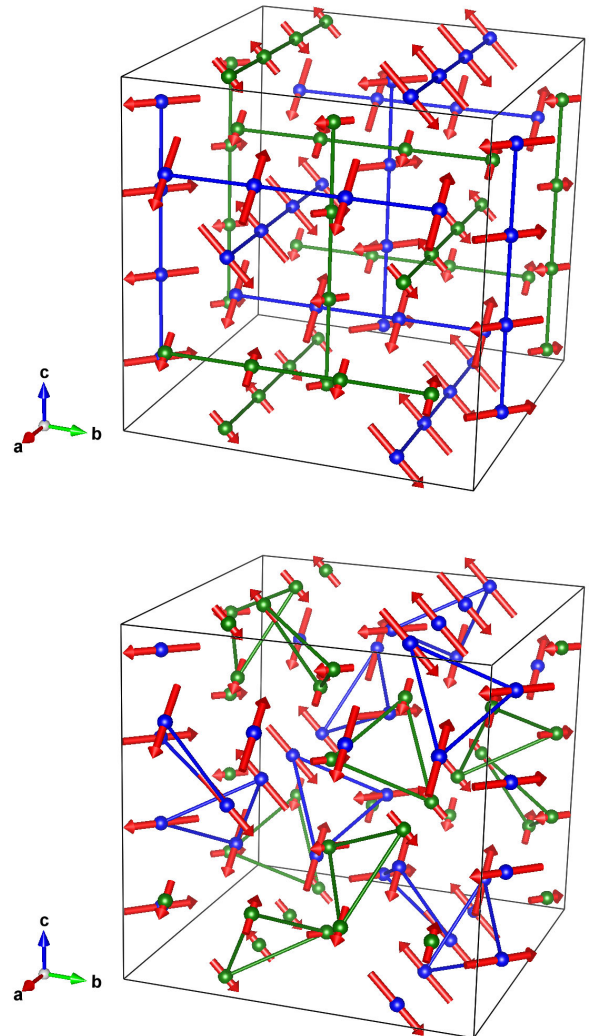


FIG. 7. Magnetic structure of  $\text{Nd}_3\text{Rh}_4\text{Sn}_{13}$  at 0.64 K, as determined from the HERMES data. The blue and green circles correspond to two inequivalent Nd-ion sites, and the arrows indicate the ordered magnetic moments. The upper panel shows bars bonding the nearest neighbor Nd ions along the principal cubic axes, and the lower panel shows triangular bonds between the second neighbors of each Nd-ion site.

observed in the single-crystal measurement at SENJU. If all the magnetic moment magnitudes were the same, the half-integer reflections would completely vanish. The lower panel shows triangular bonds between the second nearest neighbors on the orthogonal chains of the Nd1 or Nd2 sublattices with the same AFM magnetic structure as in the upper panel. The triangular lattice planes parallel to the (1, 1, 1) plane comprise a so-called 120° AFM structure, in which the magnetic moments lie within the triangular plane. The directions of magnetic moments on the other triangles are out of the plane.

We also performed a least-squares fitting analysis of the dataset of SENJU to confirm the above-described AFM ordered structure model using the single-crystal structural refinement algorithm of the software FULLPROF. Before the fitting analysis procedure, the integrated intensities were evaluated using the software STARGAZER for the reduction of the pulsed-neutron ToF data at SENJU [43]. A simple correction for neutron absorption was applied by considering the sample diameter and the neutron wavelengths, which vary with respect to the reflections in the ToF technique. Because of the noncentrosymmetric chiral cubic structure, eight magnetic domains should be considered; the [1 1 1] direction shown in Fig. 7 was rotated about the [0 0 1] axis to other threefold axes, and the four structures were inverted with respect to the origin to the chiral-structure enantiomers. To avoid a divergence in the fitting procedure, equal populations of the magnetic domains was assumed. According to this simple data treatment, the obtained magnetic moments are  $1.93(65)\mu_B/\text{Nd}$  and  $0.67(40)\mu_B/\text{Nd}$  at the Nd1 and Nd2 sites, respectively. The obtained ordered magnetic moment magnitudes, although the ambiguities are larger, are consistent with the CEF analysis results and the powder ND data analysis within the measurement accuracy. Thus, the magnetic structure comprising the inequivalent magnetic moments shown in Fig. 7 is concluded again.

## V. DISCUSSIONS

The  $I2_13$  structure of  $\text{Nd}_3\text{Rh}_4\text{Sn}_{13}$  was confirmed in the  $I'$  phase below the transition temperature  $T_D = 338$  K, which is lower than 350 K of  $\text{Ln}_3\text{Rh}_4\text{Sn}_{13}$  ( $\text{Ln} = \text{La}$  and  $\text{Ce}$ ). A previous study on the structural phase transition of  $\text{Nd}_3\text{Co}_4\text{Sn}_{13}$  reported  $T_D = 120$  K, which is also lower than 160 K of  $\text{Ln}_3\text{Co}_4\text{Sn}_{13}$  ( $\text{Ln} = \text{La}$  and  $\text{Ce}$ ). As revealed in previous studies,  $T_D$  is lower for the smaller transition-metal elements; thus, the smaller the unit-cell volume, the lower the structural transition temperature. The reduction in  $T_D$  in the Nd-based compounds can be attributed to the lanthanide contraction. As listed in the Supplemental Material [44], the Sn atoms located at the 2a and 24k sites in the I-phase structure ( $Pm\bar{3}n$ ) exhibit large thermal displacement amplitudes, and the structural transformation comprises the dominant displacements of these Sn atoms. Volume contraction caused by the smaller Nd-ion radius suppresses the free displacement space; thus, the structural instability is also suppressed to lower temperatures.

The previous structural investigation for  $\text{Nd}_3\text{Co}_4\text{Sn}_{13}$  revealed the same modulation wave vector  $\mathbf{q}_L = (1/2, 1/2, 0)$  as in the investigation for  $\text{Nd}_3\text{Rh}_4\text{Sn}_{13}$ . Although structural refinement was not attempted for  $\text{Nd}_3\text{Co}_4\text{Sn}_{13}$ , it is naturally

expected that  $\text{Nd}_3\text{Co}_4\text{Sn}_{13}$  also undergoes a chiral structural phase transition. This fact indicates that the magnetic ordered structure of  $\text{Nd}_3\text{Co}_4\text{Sn}_{13}$  should comprise two inequivalent magnetic moments at the Nd1 and Nd2 sites. In addition, we have initiated a study on  $\text{Nd}_3\text{Ir}_4\text{Sn}_{13}$ , which also shows a similar crystal structure and magnetic ordering phase transitions [36]; thus, the Nd-based 3-4-13 materials share the same structural and magnetic symmetries.

The magnetic ordered structure below  $T_N = 1.65$  K comprises the magnetic moments perpendicular to the one-dimensional Nd-ion chain along the CEF quantization axis. We performed a mean-field calculation of the XY-type magnetic exchange interaction of 0.1 meV between the nearest neighbors along the Nd-ion chains using the determined CEF schemes. Calculated ordering temperatures for Nd1 and Nd2 are 2.6 and 1.2 K, respectively, which are close to  $T_N = 1.65$  K. The calculated ordered magnetic moment magnitudes for Nd1 and Nd2 are  $1.49\mu_B/\text{Nd}$  and  $1.01\mu_B/\text{Nd}$ , respectively, which are close to the magnetic moment magnitudes  $2.15(19)\mu_B$  and  $1.12(19)\mu_B$  determined in ND. The discrepancy is caused by the symmetry assumption of the CEF Hamiltonian [Eq. (1)], which is insufficient to reproduce the INS data and the simple mean-field model based only on the nearest-neighbor interaction. Therefore, a 4f-electronic superlattice structure is concluded for the ground state of  $\text{Nd}_3\text{Rh}_4\text{Sn}_{13}$ .

A previous study on  $\text{Nd}_3\text{Co}_4\text{Sn}_{13}$  discussed the possibility of magnetically geometrical frustration [33]. The ratios of  $|\Theta|$  and  $T_D$  of  $\text{Nd}_3\text{Co}_4\text{Sn}_{13}$  and  $\text{Nd}_3\text{Rh}_4\text{Sn}_{13}$  are  $11.1/2.1 = 5.3$  and  $13.7/1.65 = 8.3$ , respectively, which are considered signatures of magnetic frustration. The nearest-neighbor magnetic moments along the cubic  $\langle 100 \rangle$  form a triangular link between the second neighbors, as shown in the bottom panel of Fig. 7. The magnetic structure on this triangle is a 120° configuration of the magnetic moments, which is typically found in other geometrically frustrated systems. The frustration feature is also observed in the magnetic susceptibility saturation above the long-range order at  $T_N = 1.65$  K, as depicted in Fig. 2(b). The AFM correlation emerges below approximately 3 K because of the susceptibility saturation; however, the magnetic frustration suppresses the long-range ordering [36]. The assumed nearest-neighbor exchange interaction of 0.1 meV in the aforementioned mean-field calculation for the ordered magnetic moment magnitudes is smaller than the Weiss temperature  $-13.7$  K. This fact may indicate that the magnetic interactions compete because of the frustration effect, and the suppressed effective interaction is in the order of 0.1 meV. The frustration mechanism in metallic systems is not simply concluded because of long-range magnetic interactions in contrast to the simple neighbor interactions. The identification of magnetic interactions using INS technique is an ongoing issue.

The chiral symmetry of crystal structures causes asymmetric Dzyaloshinskii-Moriya (DM) interaction. Considering the twofold rotation axis bisecting the middle of the Nd ions on the chain shown in Figs. 6 and 7, the Hamiltonian  $\mathcal{H} = \sum_{i,j} \mathbf{D}_{ij} \cdot (\mathbf{S}_i \times \mathbf{S}_j)$  results in the tilting of the magnetic moments toward the chain direction, and may enhance the magnetic frustration via the competing interaction. However, the observed tiny magnetic reflections do not allow the

evaluation of the tilting of the magnetic moments from the determined collinear AFM structure.

A theoretical argument has proposed the bulk chiral fermion and the Weyl semimetallic state realized in the chiral space groups [1]. Orbital Weyl points on the Brillouin-zone boundary intrinsically appear for the chiral space groups. Such a topological electronic state has been revealed as the Weyl-Kondo semimetal behavior in the isomorphic chiral Remeika phase material  $\text{Ce}_3\text{Rh}_4\text{Sn}_{13}$  [24]. The broken time reversal symmetry in addition to the chirality, as in the present Nd-based 3-4-13 systems, results in a nontrivial topological electronic state. It is an attractive subject to investigate whether the Weyl fermion carriers at the node of the linear band crossing points contribute to the magnetic interactions between the magnetic ions. The theoretical approach suggested that the internode process and the spin-momentum locking significantly influence the RKKY interactions [2]. The derived interactions represented as a Heisenberg, an Ising, and DM types are expected to provide various magnetic textures. Further investigation of the topological effects on the magnetic interactions in the Nd-based 3-4-13 systems is required, which can be approached by performing magnetic excitation measurements using an INS technique.

## VI. SUMMARY

In summary, we observed the crystal superlattice formation below  $T_D \simeq 338$  K and the AFM ordering below  $T_N = 1.65$  K in single-crystalline samples of  $\text{Nd}_3\text{Rh}_4\text{Sn}_{13}$  synthesized using the Sn-flux method. The superlattice structure was characterized by the same reduced wave vector  $\mathbf{q}_L = (1/2, 1/2, 0)$  as that for  $\text{Ln}_3\text{Tr}_4\text{Sn}_{13}$  ( $\text{Ln} = \text{La}$  and  $\text{Ce}$ ;  $\text{Tr} = \text{Co}$ ,  $\text{Rh}$ , and  $\text{Ir}$ ). This study proposes that the low-temperature phase is a chiral cubic structure characterized by the  $I2_13$

space group. The AFM ordered state below  $T_N = 1.65$  K is characterized by the orthogonal Nd-ion AFM chains connected via a triangular lattice that maintains the frustration effect. Similar sequential phase transitions are also reported for  $\text{Nd}_3\text{Co}_4\text{Sn}_{13}$  and  $\text{Nd}_3\text{Ir}_4\text{Sn}_{13}$  even though the low temperature crystal structure has not yet been identified. In addition, we propose that the Nd-based 3-4-13 systems are electronic systems in which spatial and time-reversal symmetries are simultaneously broken.

## ACKNOWLEDGMENTS

We thank D. Hashimoto, M. Shiozawa, S. Suzuki, and K. Gunji for their collaboration on the sample synthesis and x-ray scattering experiments. T. Taniguchi, M. Ohkawara, R. Sugiyura, and W. Kurosawa are acknowledged for their assistance in the low-temperature ND experiments at HERMES, JRR-3. R. Kiyonagi is also acknowledged for his assistance in the experiment at SENJU (BL18), J-PARC. We acknowledge support from the Center of Neutron Science for Advanced Materials, Institute for Materials Research, Tohoku University. The neutron industrial use project at J-PARC MLF organized by the Ibaraki Prefectural Government is also acknowledged for its financial support. This study was supported in part by JSPS KAKENHI: JP18H01182 [Scientific Research (B)], JP20H01848 [Scientific Research (B)], JP21H03732 [Scientific Research (B)], JP22H05145 [Grant-in-Aid for Transformative Research Areas (A)], JP23H04867 [Grant-in-Aid for Transformative Research Areas (A)], Yamada Science Foundation, and JST (Grant No. JPMJFR202V). The synchrotron x-ray scattering measurement at PF (2019G568), the neutron scattering experiment at J-PARC MLF (2020B0098, 2020B0112, and 2021B0093), and the powder ND at JRR-3 (22620) were performed according to the approved proposals.

- 
- [1] J. L. Mañes, *Phys. Rev. B* **85**, 155118 (2012).
- [2] H.-R. Chang, J. Zhou, S.-X. Wang, W.-Y. Shan, and D. Xiao, *Phys. Rev. B* **92**, 241103(R) (2015).
- [3] J. Hodeau, M. Marezio, J. Remeika, and C. Chen, *Solid State Commun.* **42**, 97 (1982).
- [4] S. Miraglia, J. Hodeau, M. Marezio, C. Laviron, M. Ghedira, and G. Espinosa, *J. Solid State Chem.* **63**, 358 (1986).
- [5] P. Bordet, D. Cox, G. Espinosa, J. Hodeau, and M. Marezio, *Solid State Commun.* **78**, 359 (1991).
- [6] J. P. Remeika, G. P. Espinosa, A. S. Cooper, H. Barz, J. M. Rowell, D. B. McWhan, J. M. Vandenberg, D. E. Moncton, Z. Fisk, L. D. Woolf, H. C. Hamaker, M. B. Maple, G. Shirane, and W. Thomlinson, *Solid State Commun.* **34**, 923 (1980).
- [7] G. P. Espinosa, *Mater. Res. Bull.* **15**, 791 (1980).
- [8] G. P. Espinosa, A. S. Cooper, and H. Barz, *Mater. Res. Bull.* **17**, 963 (1982).
- [9] R. Gumeniuk, in *Handbook on the Physics and Chemistry of Rare Earths*, edited by J.-C. G. Bünzli and V. K. Pecharsky (Elsevier Science, North-Holland, 2018), Vol. 54, p. 43–143.
- [10] M. F. Hundley, J. L. Sarrao, J. D. Thompson, R. Movshovich, M. Jaime, C. Petrovic, and Z. Fisk, *Phys. Rev. B* **65**, 024401 (2001).
- [11] A. L. Cornelius, A. D. Christianson, J. L. Lawrence, V. Fritsch, E. D. Bauer, J. L. Sarrao, J. D. Thompson, and P. G. Pagliuso, *Physica B* **378-380**, 113 (2006).
- [12] A. Ślebarski, B. D. White, M. Fijałkowski, J. Goraus, J. J. Hamlin, and M. B. Maple, *Phys. Rev. B* **86**, 205113 (2012).
- [13] E. Lyle Thomas, H.-O. Lee, A. N. Bankston, S. MaQuilon, P. Klavins, M. Moldovan, D. P. Young, Z. Fisk, and J. Y. Chan, *J. Solid State Chem.* **179**, 1642 (2006).
- [14] A. Ślebarski and J. Goraus, *Phys. Rev. B* **88**, 155122 (2013).
- [15] U. Köhler, A. P. Pikul, N. Oeschler, T. Westerkamp, A. M. Strydom, and F. Steglich, *J. Phys.: Condens. Matter* **19**, 386207 (2007).
- [16] M. Gamża, W. Schnelle, A. Ślebarski, U. Burkhardt, R. Gumeniuk, and H. Rosner, *J. Phys.: Condens. Matter* **20**, 395208 (2008).
- [17] H. Sato, T. Fukuhara, S. Iwakawa, Y. Aoki, I. Sakamoto, S. Takayanagi, and N. Wada, *Phys. B: Condens. Matter* **186-188**, 630 (1993).
- [18] S. Takayanagi, H. Sato, T. Fukuhara, and N. Wada, *Phys. B: Condens. Matter* **199-200**, 49 (1994).
- [19] J. R. Collave, H. A. Borges, S. M. Ramos, E. N. Hering, M. B. Fontes, E. Baggio-Saitovitch, A. Eichler, E. M. Bittar, and P. G. Pagliuso, *Solid State Commun.* **177**, 132 (2014).

- [20] Y. Otomo, K. Iwasa, K. Suyama, K. Tomiyasu, H. Sagayama, R. Sagayama, H. Nakao, R. Kumai, and Y. Murakami, *Phys. Rev. B* **94**, 075109 (2016).
- [21] K. Suyama, K. Iwasa, Y. Otomo, K. Tomiyasu, H. Sagayama, R. Sagayama, H. Nakao, R. Kumai, Y. Kitajima, F. Damay, J.-M. Mignot, A. Yamada, T. D. Matsuda, and Y. Aoki, *Phys. Rev. B* **97**, 235138 (2018).
- [22] S. Nakazato, K. Iwasa, D. Hashimoto, M. Shiozawa, K. Kuwahara, H. Nakao, H. Sagayama, M. Ishikado, T. Ohhara, A. Nakao, K. Munakata, and R. Kiyonagi, *JPS Conf. Proc.* **30**, 011128 (2020).
- [23] K. Iwasa, S. Nakazato, D. Hashimoto, M. Shiozawa, K. Kuwahara, H. Sagayama, S. Ohira-Kawamura, N. Murai, D. T. Adroja, and A. M. Strydom, *J. Phys. Soc. Jpn.* **90**, 124701 (2021).
- [24] K. Iwasa, K. Suyama, S. Ohira-Kawamura, K. Nakajima, S. Raymond, P. Steffens, A. Yamada, T. D. Matsuda, Y. Aoki, I. Kawasaki, S.-I. Fujimori, H. Yamagami, and M. Yokoyama, *Phys. Rev. Mater.* **7**, 014201 (2023).
- [25] H.-H. Lai, S. E. Grefe, S. Paschen, and Q. Si, *Proc. Natl. Acad. Sci. USA* **115**, 93 (2018).
- [26] S. E. Grefe, H.-H. Lai, S. Paschen, and Q. Si, *Phys. Rev. B* **101**, 075138 (2020).
- [27] D. M. Kirschbaum, M. Lužnik, G. Le Roy, S. Paschen, *J. Phys. Mater.* **7**, 012003 (2024).
- [28] Y. W. Cheung, J. Z. Zhang, J. Y. Zhu, W. C. Yu, Y. J. Hu, D. G. Wang, Y. Otomo, K. Iwasa, K. Kaneko, M. Imai, H. Kanagawa, K. Yoshimura, and S. K. Goh, *Phys. Rev. B* **93**, 241112(R) (2016).
- [29] J. Welsch, S. Ramakrishnan, C. Eisele, N. van Well, A. Schönleber, S. van Smaalen, S. Matteppanavar, A. Thamizhavel, M. Tolkiehn, C. Paulmann, and S. Ramakrishnan, *Phys. Rev. Mater.* **3**, 125003 (2019).
- [30] V. Kozii and L. Fu, *Phys. Rev. Lett.* **115**, 207002 (2015).
- [31] Y. Wang, G. Y. Cho, T. L. Hughes, and E. Fradkin, *Phys. Rev. B* **93**, 134512 (2016).
- [32] C. W. Wang, C. N. Kuo, H. F. Liu, C. S. Lue, L. M. Wang, J. W. Lin, K. C. Rule, and J. S. Gardner, *Phys. B: Condens. Matter* **551**, 12 (2018).
- [33] C. W. Wang, J. W. Lin, C. S. Lue, H. F. Liu, C. N. Kuo, R. A. Mole, and J. S. Gardner, *J. Phys.: Condens. Matter* **29**, 435801 (2017).
- [34] C. Nagoshi, R. Yamamoto, K. Kuwahara, H. Sagayama, D. Kawana, M. Kohgi, H. Sugawara, Y. Aoki, H. Sato, T. Yokoo, and M. Arai, *J. Phys. Soc. Jpn.* **75**, 044710 (2006).
- [35] J. R. L. Mardegan, N. Aliouane, L. N. Coelho, O. Agüero, E. M. Bittar, J. C. Lang, P. G. Pagliuso, I. L. Torriani, and C. Giles, *IEEE Trans. Magn.* **49**, 4652 (2013).
- [36] A. Shimoda, K. Iwasa, K. Kuwahara, H. Sagayama, H. Nakao, M. Ishikado, T. Ohhara, A. Nakao, A. Hoshikawa, and T. Ishigaki, *JPS Conf. Proc.* **38**, 011091 (2023).
- [37] L. J. Farrugia, *J. Appl. Cryst.* **32**, 837 (1999).
- [38] K. Nakajima, S. Ohira-Kawamura, T. Kikuchi, M. Nakamura, R. Kajimoto, Y. Inamura, N. Takahashi, K. Aizawa, K. Suzuya, K. Shibata, T. Nakatani, K. Soyama, R. Maruyama, H. Tanaka, W. Kambara, T. Iwahashi, Y. Itoh, T. Osakabe, S. Wakimoto, K. Kakurai, F. Maekawa, M. Harada, K. Oikawa, R. E. Lechner, F. Mezei, and M. Arai, *J. Phys. Soc. Jpn.* **80**, SB028 (2011).
- [39] Y. Inamura, T. Nakatani, J. Suzuki, and T. Otomo, *J. Phys. Soc. Jpn.* **82**, SA031 (2013).
- [40] I. Tamura, K. Oikawa, T. Kawasaki, T. Ohhara, K. Kaneko, R. Kiyonagi, H. Kimura, M. Takahashi, M. Arai, Y. Noda, and K. Ohshima, *J. Phys.: Conf. Ser.* **340**, 012040 (2012).
- [41] K. Oikawa, T. Kawasaki, T. Ohhara, R. Kiyonagi, K. Kaneko, I. Tamura, T. Nakamura, M. Harada, A. Nakao, T. Hanashima, K. Munakata, H. Kimura, Y. Noda, M. Takahashi, and T. Kiyotani, *JPS Conf. Proc.* **1**, 014013 (2014).
- [42] T. Ohhara, R. Kiyonagi, K. Oikawa, K. Kaneko, T. Kawasaki, I. Tamura, A. Nakao, T. Hanashima, K. Munakata, T. Moyoshi, T. Kuroda, H. Kimura, T. Sakakura, C.-H. Lee, M. Takahashi, K. Ohshima, T. Kiyotani, Y. Noda, and M. Arai, *J. Appl. Cryst.* **49**, 120 (2016).
- [43] T. Ohhara, K. Kusaka, T. Hosoya, K. Kurihara, K. Tomoyori, N. Niimura, I. Tanaka, J. Suzuki, T. Nakatani, T. Otomo, S. Matsuoka, K. Tomita, Y. Nishimaki, T. Ajima, and S. Ryufuku, *Nucl. Instrum. Methods Phys. Res. Sect. A* **600**, 195 (2009).
- [44] See Supplemental Material at <http://link.aps.org/supplemental/10.1103/PhysRevB.109.134425> for the structural refinements based on the synchrotron diffraction data taken at BL-8A of Photon Factory, KEK.
- [45] K. Momma and F. Izumi, *J. Appl. Cryst.* **41**, 653 (2008).
- [46] K. Iwasa, Y. Otomo, K. Suyama, K. Tomiyasu, S. Ohira-Kawamura, K. Nakajima, and J.-M. Mignot, *Phys. Rev. B* **95**, 195156 (2017).
- [47] U. Walter, *J. Phys. Chem. Solids* **45**, 401 (1984).
- [48] W. Marshall and R. D. Lowde, *Rep. Prog. Phys.* **31**, 705 (1968).
- [49] G. Aeppli and C. Broholm, in *Handbook on the Physics and Chemistry of Rare Earths*, edited by K. A. Gschneidner, Jr., L. Eyring, G. H. Lander, and G. R. Choppin (Elsevier Science, North-Holland, 1994), Vol. 19, pp. 123–175.
- [50] M. Arai, A. D. Taylor, S. M. Bennington, Z. A. Bowden, R. Osborn, M. Kohgi, K. Ohoyama, and T. Nakane, *Proc. ICANS-XI* **644** (1990), <http://www.neutronresearch.com/proc/?c=199001;o=0>.
- [51] R. Kajimoto, K. Sato, Y. Inamura, and M. Fujita, *AIP Conf. Proc.* **1969**, 050004 (2018).
- [52] J. Rodríguez-Carvajal, *Phys. B: Condens. Matter* **192**, 55 (1993).